Array feature size influences nucleic acid surface capture in DNA microarrays

David S. Dandy, Peng Wu, and David W. Grainger

PNAS published online May 7, 2007;
doi:10.1073/pnas.0606054104

Array feature size influences nucleic acid surface capture in DNA microarrays

David S. Dandy*, Peng Wu†, and David W. Grainger†‡

Departments of *Chemical and Biological Engineering and †Chemistry, Colorado State University, Fort Collins, CO 80523

Edited by Charles R. Cantor, Sequenom, Inc., San Diego, CA, and approved March 23, 2007 (received for review July 19, 2006)

Analyte affinity capture by surface-immobilized diagnostic agents is a routinely used assay format for profiling numerous medically and technologically important target analytes. These assays suffer from numerous performance limitations, including sensitivity and rapidity. Assay miniaturization is advocated to improve surface-capture performance, specifically exploiting the inverse relationship between analyte flux and capture feature size under mass transfer-limiting capture conditions that characterize many such assay formats. Reduced capture feature sizes, e.g., microarrays, are proposed to overcome mass transfer limitations, yet this is difficult to achieve across several size scales. This study validates certain advantages advocated for capture spot miniaturization using a rationale to understand surface capture miniaturization strategies. Experimentally derived immobilized ligand and target capture densities as a function of microspot size for DNA oligomers immobilized on model gold substrates are compared directly with theoretical analysis, validating the hypothesis that miniaturization yields many practical assay advantages. Specifically, results show that transitions from assay mass transfer limiting to kinetically limiting conditions as feature size decreases identify an optimal microspot size range for a specific bioassay system. Analytical advantages realized from such assay miniaturization are more uniform target-spot coverage and substantially increased rate of capture (hybridization), increasing assay signal and rapidity.

bioassay | mass transport | miniaturization

New strategies to improve bioanalytical methods, clinical assay designs, diagnostic devices, and rapid screening tools for disease biomarkers, biosecurity threats, and food pathogens have nearly universally emphasized miniaturization as a route to improve performance, cost, convenience, speed-to-answer, and portability. Reducing size scales for these applications has many practical implications to the measurement of biological analytes and such assay designs. Optimal device sizing is a key design feature for assays that commonly involve affinity binding of analytes to surfaces. Surface capture microassays employ diverse affinity reagents (e.g., antibodies, aptamers, and DNA) to capture broad varieties of analytes (e.g., small molecules, peptides, proteins, nucleic acids, and pathogens). Without active transport (e.g., stirring or field-induced), all current microassay platforms suffer from severe mass transfer limitations, that is, rates of analyte transport to the assay capture surface significantly lag rates of analyte binding. This problem is particularly important in producing rapid results in DNA microassays, where resulting DNA–DNA charge–charge interactions produce complications. A long-standing yet experimentally tentative assertion is that surface capture assays benefit significantly from reduced capture feature (i.e., microarray spot) size, specifically, that these assay systems capitalize on the inverse relationship between analyte flux and capture feature size under mass transfer limiting conditions (1, 2). It is demonstrated here that the assertion is correct but not exclusively as a result of this flux behavior associated with the mass transfer limit. Instead, a tremendous enhancement in nucleic acid hybridization rate and capture yield may be realized as assay feature size decreases through mitigation of mass transfer limitations. Additionally, fractional feature capture capacity and coverage uniformity for analyte capture are both also predicted to increase with decreasing spot size. Although this offers rational design improvements to guide current microassays, actual performance advantages based on such scaling are not fully experimentally exploited. To date, the microarray assay format remains largely a research tool, with several chemometric reliability and sensitivity issues outstanding. However, the recent multiinvestigator Microarray Quality Control Taskforce report (3) suggests that such issues might be overcome by using standardized protocols.

One early hypothesis advocating assay miniaturization claims that surface-capture assay signal increases as immobilized surface-capture affinity ligand area decreases, reaching, for example, a signal/noise ratio maximum of ≈60 as immobilized capture antibody (dissociation constant $K_D \approx 10^{-11}$ M) density approaches zero, i.e., immobilized spot size approaches zero (4). Although details of this largely theoretical proposal are deferred to a substantial precedent literature, full experimental validation of this scaling prediction has not yet been performed. One reason is that this previous miniaturization model required *a priori* assumptions regarding scale-dependent microspot assay sensitivity and a uniform and known surface immobilization density of surface-capture ligand. The present experimental and modeling work is free of such restrictive assumptions, and we now present such a validation by exploiting size scaling for immobilized thiolated oligomer DNA probes on planar gold surfaces as a model. Experimentally derived immobilized ligand and target capture densities as a function of microspot size are compared directly with theoretical analysis that validates the hypothesis that miniaturization yields practical assay advantages. Specifically, it is demonstrated that the transition from mass-transfer-limiting to kinetic-limiting conditions as feature size decreases may be applied to identify optimal microspot size ranges for specific assays. The advantages realized from miniaturization are more uniform target coverage on the feature and substantially increased rate of binding or hybridization, increasing assay signal.

Results

Spot Size Dependence. Terminally thiolated 20-mer DNA oligonucleotide probes were immobilized on fabricated gold surface structures of different diameters, followed by hybridization with complementary target DNA. Tethering of thiolated nucleic acids to gold surfaces has been widely reported (5–14), providing a well characterized, readily scaled, quasi-two dimensional surface

Author contributions: D.S.D., P.W., and D.W.G. designed research; D.S.D. and P.W. performed research; D.S.D., P.W., and D.W.G. analyzed data; and D.S.D., P.W., and D.W.G. wrote the paper.

The authors declare no conflict of interest.

This article is a PNAS Direct Submission.

Abbreviation: MCU, 11-mercapto-1-undecanol.

‡To whom correspondence should be sent at the present address: Department of Pharmaceutics, University of Utah, Salt Lake City, UT 84112. E-mail: david.grainger@utah.edu.

This article contains supporting information online at www.pnas.org/cgi/content/full/0606054104/DC1.

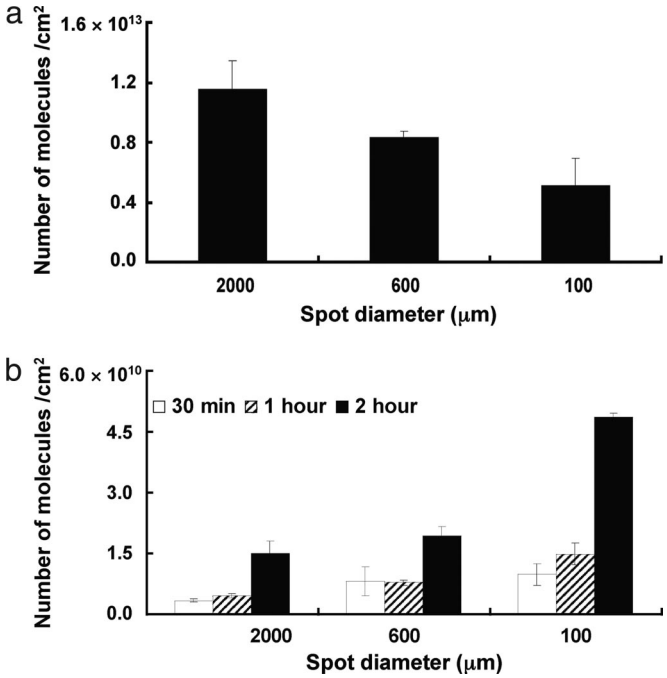

Fig. 1. Comparisons of nucleic acid microarray feature occupancies with probes and hybridized 20-mer targets as a function of array feature size. Surface density of DNA probe immobilized on gold features of different sizes (*a*), and hybridized complementary target ($n \geq 3$ spots) calculated from ^{32}P-labeled 20-mer oligonucleotide probes and complementary targets (*b*).

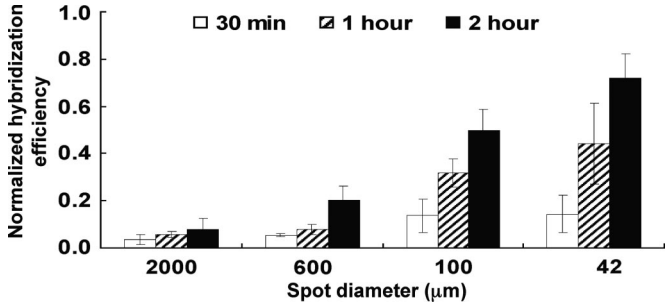

Fig. 2. Normalized fractional coverage of complementary target DNA to immobilized DNA probe on gold surface features of various diameters ($n \geq 3$ spots) taken from fluorescence imaging results. Cy3-labeled 20-mer oligonucleotide probe and Cy5-labeled complementary target were used to compare hybridization efficiency ($n \geq 3$ spots).

capture model to study DNA hybridization efficiency. As DNA thiols form surface adlayers with reliable thermodynamic stability and reproducible density, fabricated gold feature size scaling can be used to produce different surface-capture feature sizes with relatively uniform DNA probe density. Both ^{32}P- and fluorescent dye-labeled oligonucleotides were used to investigate DNA immobilization and hybridization. [^{32}P]DNA experiments provide an absolute surface density of immobilized DNA probes and captured targets. Fluorescence imaging provides relative intensities for tethered and captured molecules on these surfaces, with ready capability to compare relative immobilization and hybridization efficiencies across different spots. Different gold spot sizes (diameters: 2 mm, 600 μm, and 100 μm) were created to compare DNA immobilization and hybridization across sizes amenable to DNA density analysis.

^{32}P-labeled identical DNA probes and targets were used to quantify immobilization and hybridization of DNA on fabricated gold features using phosphor imaging (6, 15). Fig. 1 shows that hybridized DNA target surface density increases substantially as gold spot diameter decreases from 2 mm to 100 μm.

Results for fluorescence intensity imaging of gold spots with thiolated DNA probes labeled with Cy3 dye and complementary target labeled with Cy5 dye (6) are shown in Fig. 2. Both probe and target fluorescent signals are sequentially scanned, and Cy5/Cy3 ratios are used to compare relative hybridization efficiencies across different feature sizes. In contrast with the data in Fig. 1*a*, probe DNA Cy3 fluorescent intensity is invariant with feature size, remaining unaffected by possible energy transfer (quenching) issues upon duplex formation [see supporting information (SI) *Materials and Methods*] due to the low fractional hybridization typical of these conditions. Fluorescence experiments produced higher background signals and larger data variance from spot to spot because of light scattering from gold surface defects (i.e., scratches and residual salt crystals). Fluorescent dye DNA labeling also introduces minor nonspecific binding (i.e., hydrophobic surface adsorption) during DNA probe immobilization and target hybridization (data not shown). However, fluorescence imaging provides improved resolution (5 μm) over phosphorus imaging (50 μm), reliably imaging signal from the smallest spot diameters (e.g., to 42 μm diameter). The more molecularly quantitative ^{32}P imaging results together with more spatially resolved integrated fluorescence surface densities for probes and targets average several gold features of the same diameter containing DNA. Despite different DNA probe and target labels, distinct data processing and experimental limitations in these two approaches, both methods yield very similar relationships between feature size and DNA hybridization efficiency, as demonstrated by Figs. 1 and 2. Although previous reports support the intuitive idea that probe crowding produces both charge and steric hindrance to hybridization efficiency (16), the observed inverse relationship is not an artifact of the probe density variations displayed in Fig. 1*a*. Within experimental error, probe densities in the fluorescence experiments are not dependent on spot size, and the hybridization results remain qualitatively consistent with the ^{32}P experiments. Moreover, early quantitative study of the surface probe density effects on hybridization (17) showed that, using 25-mer strands, hybridization rates fall into the same kinetic regime for probe densities between 5×10^{12} and 1.2×10^{13} cm^{-2} (the probe density range used here). Consistent with this result, as discussed in *Materials and Methods*, a single solid-phase hybridization rate constant was identified in the reaction diffusion model such that it was not necessary to vary this parameter with spot size to quantitatively replicate the ^{32}P experiments.

The most significant result of this study is represented by the quantitative data in Fig. 1*b*, which are further supported qualitatively by the fluorescence data in Fig. 2. Previous theoretical assertions that capture efficiencies (fractional occupancies) depend inversely on capture feature size (4) are indeed borne out by these results. Although the data in Fig. 1*b* correspond to absolute target densities, the results shown in Fig. 3 definitively show that average hybridization efficiency increases as capture spot size decreases. After 2 h of incubating the target with immobilized probe, the largest features reach 10–20% of equilibrium coverage, whereas the smallest spots achieve 60–80% of equilibrium hybridization efficiency (for this system, ≈1% of available probes).

Particular values reported here are specific to the system (e.g., DNA 20-mers on gold) and assay conditions used in this study, but the general trends in Fig. 3 are the same as predicted by the model for a wide range of dissociation constants, diffusion coefficients, initial target concentrations, and probe–target combinations.

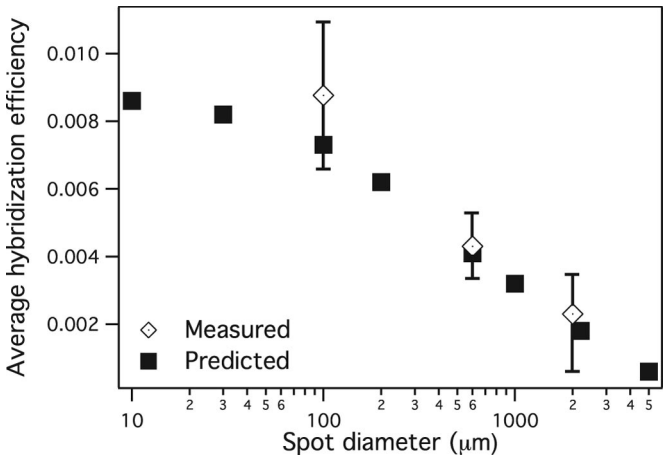

Fig. 3. Average hybridization efficiency (fractional coverage) after 2 h of incubating target with immobilized probe as a function of spot size. Diamonds represent data collected by [^{32}P]DNA signal of probe and target, and squares represent the results of the reaction–diffusion model.

Intraspot Gradients. Fig. 1*a* represents average probe densities for each of the three spot sizes. The phosphor imager's 50-μm resolution allows probe coverage quantitation as a function of position on the 2-mm spots. [^{32}P]DNA signals from immobilized probes were collected along multiple radial lines across these spots and averaged. Probe coverage is not uniform across the 2-mm spot surface, as indicated by the symbols in Fig. 4. To rigorously model target hybridization through application of analyte and hybridized probe mass conservation boundary conditions at spot surfaces (Eqs. **2** and **3** in *SI Materials and Methods*), it is therefore necessary to capture this radial dependence in mathematical form; to that end, a simple nonlinear least-squares fit is applied to the data, resulting in the curve in Fig. 4.

As with the probe data in Fig. 1*a*, the results in Figs. 1*b* and 2 represent average hybridization efficiencies for each spot size at three time points. Collecting ^{32}P-labeled DNA signals from hybridized target along multiple radial lines on the 2-mm spots and ratioing this result with data in Fig. 4 allows the determination of variations in hybridization efficiency across spot surfaces. As indicated by the symbols in Fig. 5 for two different time points, hybridization efficiency monotonically increases from spot center to outer edge. Thus, probe (Fig. 4) and target (data not shown) densities both decrease monotonically from the spot center to the outer edge for 2-mm spots, but the ratio of these two quantities manifests an inverse trend. Because probe and hybridized target densities both decrease with radial position, the rise in hybridization efficiency cannot be explained by what is, in effect, a smaller denominator. The fact that the kinetics should not vary across the spot (17) indicates that transport to the surface may be responsible. To explain this radial dependence, probe coverage dependence in Fig. 4 is incorporated into the reaction–diffusion model described in *Discussion* (and represented by Eqs. **1–3** in *SI Materials and Methods*). The curves shown in Fig. 5 were obtained by a numerical solution of the transient diffusion equation and boundary conditions, using parameters specified in *Materials and Methods*.

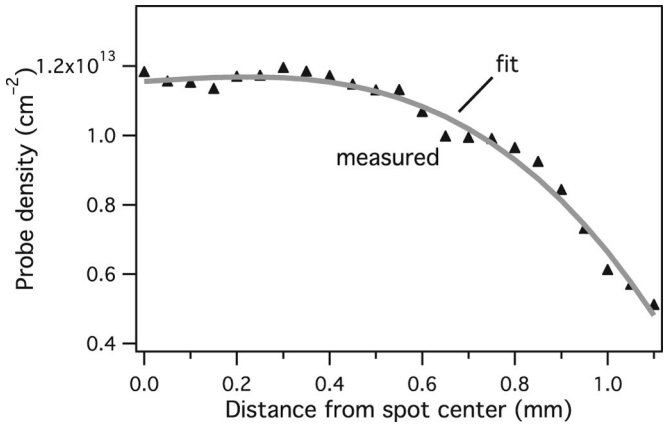

Fig. 4. Surface density profile of immobilized DNA probe on a 2-mm spot as a function of distance from spot center (symbols) and an accompanying polynomial fit used in the reaction–diffusion model (curve).

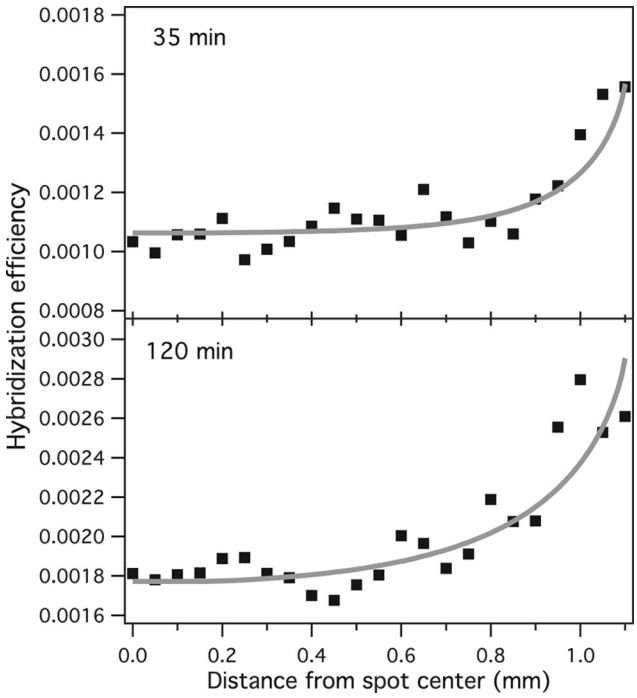

Fig. 5. Hybridization efficiency as a function of radial position on the spot surface for 35- and 120-min DNA target incubations on the 2-mm probe spots. Symbols represent averages of replicate data collected from ^{32}P signals, and curves are predictions from the reaction–diffusion model.

Discussion

Combining a full reaction–diffusion numerical model with DNA oligomer/gold spot experiments, our results (Fig. 3) directly demonstrate that the surface fractional occupancy rate increases when the microspot surface area decreases (4). In addition, the radial occupancy gradient from microspot center to edge is predicted to decrease as feature surface area decreases, producing more uniform probe/analyte binding within smaller microspots. Monotonic increase in fractional coverage with radial position, as shown in Fig. 5, is a consequence of mass-transfer-limited conditions associated with the larger spots used in this study. Across the entire feature, the numerical model predicts that target concentration remains low, $\approx$1% of the bulk concentration, in the vicinity of the spot's surface, even after 2 h of hybridization. This vanishing target concentration behavior at the surface, that is, formation of an analyte depletion layer, is consistent with mass-transfer-limiting conditions. Near the spot center, target is delivered to the surface solely through the linear diffusion component, whereas, toward the outer edge, a lateral (radial) component of diffusive flux augments the linear com-

ponent, producing hemispherical diffusion, resulting in a net rate increase for target transport to the feature. This scale-dependent, mass-transfer-limiting behavior is analogous to that recognized for microelectrodes (18), as first characterized by Saito (19). Put another way, the region on the feature near the outer edge samples more target through greater proximate fluid volume than does the region near the center. This radial occupancy gradient diminishes as the feature size diminishes, eventually becoming flat (uniform) over the surface (data not shown). Specific reasons for this behavior center on the transition from mass-transfer-limiting to kinetic-limiting conditions as the feature size decreases. Transition from one limit to the other is discussed in more detail below; here, the effect manifests itself as a gradual disappearance of the target depletion layer to the point where the solution target concentration is uniform across the feature surface and close in value to its concentration away from the surface. Physically, the region near the spot center dependent on linear diffusion decreases with spot size to the point at which transport is essentially hemispherical (i.e., linear and radial, where linear contributions are comparable with radial contributions) when the feature is small enough. Thus, purely from the perspective of enhancing hybridization efficiency uniformity across the feature, it is desirable to decrease its size toward this transition point in rate mechanisms.

In general, the smaller the magnitude of the dissociation constant K_D or initial target concentration C_{To}, the higher the assay sensitivity to feature size; that is, the degree of mass transfer limitation impacts the degree to which spot size dependence is exhibited. At one extreme, for very efficient hybridization and vanishingly small target concentrations, even submicrometer-scale spots may be subjected to mass transfer limitations. At the other extreme, if binding or hybridization rates are low and target concentrations are large, all capture features, regardless of size, will be kinetically limited with little or no dependence of hybridization efficiency on spot size. Most microarrays and assays, however, operate somewhere between these two extremes. Results in Fig. 3 illustrate this intermediate behavior. After 2 h of hybridization, an approximately exponential dependence of efficiency on feature size remains for spots diameters of >200–300 μm, whereas hybridization efficiency on features smaller than this display decreasing sensitivity to capture spot size. This may be examined further by using a central tenet of the hypothesis applied to predict the phenomenon now confirmed by this work, specifically that smaller spots capture target analyte faster than larger spots because of an expression relating the target analyte surface flux q (mol·cm^{-2}·s^{-1}) to the capture spot radius a as $q = 2DC_{To}/\pi a$ (1, 2), where D is the target effective binary diffusion coefficient. This expression for the target flux onto the surface may be derived from the mass-transfer-limiting expression for target concentration distribution (see *SI Materials and Methods*) and is valid only at the spot center. As shown above, under mass-transfer-limiting conditions, flux does not remain constant across the spot surface but monotonically increases with radial distance from the center. To investigate whether the system under study does, indeed, suffer from mass transfer limitations, results of the full reaction–diffusion model were applied to predict the flux at the center of the feature, as shown in Fig. 6. Circle symbols represent results obtained from the numerical solution to the reaction-diffusion model; the dashed line is a nonlinear regression of that data, assuming the $q \propto a^{-1}$ relationship. Consistent with hybridization efficiency data of Fig. 3, the predicted target flux at the spot center indicates mass-transfer-limiting behavior in the system for features of >200–300 μm. However, for features smaller than this, the system transitions to kinetic-limited behavior. As this transition occurs, the actual hybridization rate becomes significantly lower than predicted by mass-transfer-limited theory. The prediction that hybridization rate and efficiency become insensitive to spot size under kinetic limitations is consistent with experimental measurements of binding kinetics in flow cells designed for operation in the kinetically limited regime (20). This previous work determined that, for spots ranging from 1,145 μm to 80 μm, fractional coverage (measured as the mean percentage of binding) was almost independent of spot size for experiments under flow up to 27 min in duration.

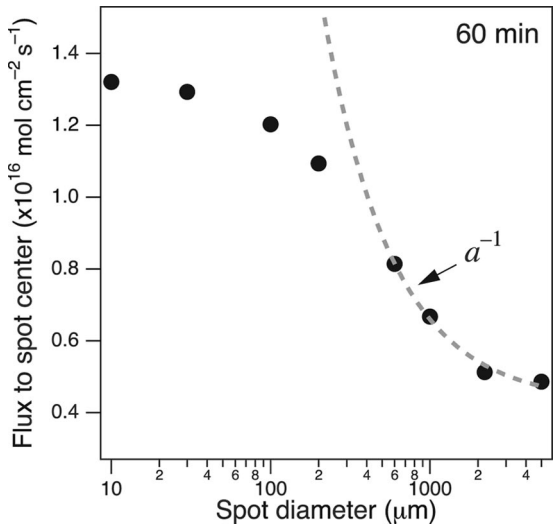

Fig. 6. Predicted target flux at the center of the immobilized probe spot (circles) as a function of feature size after 1 h of hybridization. The dashed line is a nonlinear regression of the data confirming the implication arising from Fig. 3 that the larger spots are mass-transfer-limited, whereas the smaller spots (≤200 μm) approach kinetically limiting behavior.

Experiments and numerical simulations support optimal feature sizes for any system that involves surface capture, binding, or hybridization of specific target analytes to affinity probes immobilized within a discrete surface region. The criterion for fractional coverage or hybridization efficiency is not its maximum, because, as shown in Fig. 3, this quantity increases monotonically up to the smallest feature size considered. Instead, the optimum feature size is the point at which the system begins to transition from mass transfer limiting to kinetic limiting behavior. When rates of diffusion and hybridization are comparable, the affinity capture system is functioning as close to ideal as possible. Further increases in capture efficiency are possible as the surface feature size is further decreased, but the technical challenges associated with engineering such features with requisite precision and acquiring sufficient signal upon hybridization may make the pursuit of additional gains problematic.

The optimal surface capture feature size may be estimated without performing hybridization studies or detailed numerical simulations, provided that necessary parametric data are available. The relative rates of hybridization and mass transfer are characterized by a dimensionless parameter, the Damköhler number, defined in this system as $Da = k_1 a C_{Po}/D$ where k_1 is the forward rate constant for solid phase hybridization and C_{Po} is the initial average probe surface density. The desired feature size is the value of a for which (approximately) $0.5 \leq Da \leq 1$, that is, conditions for which the assay system displays slightly kinetic-limiting behavior. By using the parameters associated with the system considered here, it is estimated that the radius, a, should be between 60 and 120 μm, consistent with the results shown in Figs. 5 and 6.

In this regard, microarray spots currently used in most commercial assay formats (50- to 200-μm diameters) are in the range of optimal size for surface capture assay in terms of probe/analyte capture efficiency. Further increases in probe/analyte

reaction efficiency by reducing feature dimensions to nanometer sizes do not promise the same assay performance enhancements as reducing size from macroscopic (e.g., approximately mm to cm diameters) to sizes of 50–200 μm because of the observed transition from mass-transfer-limiting behavior to kinetic-limited behavior in the range of microarray spot sizes. However, nanometer-to-micrometer surface-capture features provide other promising characteristics other than improved assay sensitivity (e.g., high feature densities, high reporting content, and integration with active transport in microanalysis systems) but also face other more technical challenges (e.g., reliable fabrication and detection). Beyond optimal surface feature size analysis, our numerical model can also be used to predict incubation/hybridization times, sensitivity, and fractional occupancy for microarray-based assays and other surface-capture bioassays before performing experiments.

Materials and Methods

Materials. All DNA oligonucleotides (TriLink, San Diego, CA) were HPLC-purified. The 20-mer oligonucleotide probe 5′-CTGAACGGTAGCATCTTGAC-3′ was selected because it forms a stable duplex with its complementary target 5′-GTCAAGATGCTACCGTTCAG-3′ (oligo2) at room temperature, with minimal interference due to self-complementarity or secondary structure (21, 22). The thiolated DNA probe [5′-terminal thiol group with a hexamethylene spacer (5′-HS-C6-oligo1-3′)] was end-labeled with ^{32}P at its 3′ terminus by using [α-^{32}P]ddATP (Amersham Biosciences, Piscataway, NJ) in the presence of terminal transferase (15); complementary target oligonucleotide 2 and noncomplementary control oligonucleotide 1 was end-labeled with ^{32}P at 5′ ends by using [γ-^{32}P]ATP (Amersham Biosciences) in the presence of T4 polynucleotide kinase (Promega, Madison, WI) (6). Labeled oligonucleotides were purified with an oligonucleotide minispin column (Roche Diagnostics, Indianapolis, IN). Concentrations of ^{32}P-labeled oligonucleotides were measured with a TriCarb 1500 liquid scintillation analyzer for specific activity determinations. For fluorescence detection, probe was 3′-thiolated (C3 propyl spacer) with a 5′-fluorescent Cy3 label (5′-Cy3-olgo1-C3-SH-3′, as received from vendor); complementary target was supplied 3′-labeled with fluorescent Cy5 dye (5′-oligo2-Cy5-3′). After probe DNA immobilization and hybridization with target DNA, fluorescent dyes on both probe and target DNA extend away from the gold substrate, minimizing gold-fluorescent dye quenching (7). 11-Mercapto-1-undecanol (MCU) (97%; Aldrich, St. Louis, MO) was used as received. The buffer 1× TE-NaCl contained 1 M NaCl, 10 mM Tris·HCl, and 1 mM EDTA (pH = 7.0). Chromium (99.5%; Aldrich) and gold wire (99.999%; Aldrich) were used to coat silicon wafers. Water from Millipore (Billerica, MA) (18 MΩ·cm) was used for all experiments.

Photolithographic Preparation of Gold Spot Arrays. Arrays of gold spots with controlled diameters (42-, 100-, 600-, and 2,000-μm diameters) were fabricated on silicon substrates by using routine photolithography. The space between spots was sufficient to avoid depletion or competition during the 2-h experiments. Semiconductor-grade polished silicon wafers were first cleaned in piranha solution for 30 min, rinsed with deionized water, and blown dry with nitrogen. A bilayer photoresist stack (Shipley 1818, LOR 10B; Microchem, Newton, MA) was spin-coated onto the wafer and exposed through a high-resolution (2,700 dpi) laser-printed positive transparency mask to irradiate the array pattern on the substrate by using UV light. This pattern was then developed according to the manufacturer's recommendations. Gold (30 nm thick) was deposited onto a 6-nm Ti adhesion layer using e-beam sputtering, after which a chemical lift-off procedure removed the photoresist layers to reveal the arrayed gold spots. The wafer was then rinsed with methanol, blown dry with nitrogen, and plasma-cleaned (O_2 and Ar) with 0.3 Torr of total pressure at 100 W for 5 min before DNA probe exposure.

^{32}P-Labeled Radiometric Assay of both DNA Surface Density and Hybridization Efficiency on Gold. Metal-coated silicon pieces with deposited gold spots of different diameters were plasma-cleaned with O_2/Ar plasma for 5 min before DNA probe exposure. To quantify immobilized DNA probe surface density, probe DNA solutions at 1 μM concentrations (^{32}P-labeled 5′-HS-C6-oligo1-3′ diluted with unlabeled identical 5′-HS-C6-oligo1-3′) were prepared in 1× TE-NaCl buffer. Substrates were immersed into DNA solutions for 5 h, rinsed copiously with 1× TE-NaCl buffer and water, dried with N_2, then backfilled with MCU (10 μM in water) for 1 h to fill vacant gold sites and prevent nonspecific DNA capture (6, 7, 15). After MCU backfilling, samples were rinsed with water, dried with N_2, and exposed to a storage phosphor imager (Amersham Biosciences) simultaneously with known [^{32}P]ATP standards for radioactivity surface measurements. To quantify the surface density of target DNA hybridization, substrates were first immersed in probe solutions containing only 5′-HS-C6-oligo1-3′ at 1 μM for 5 h, then rinsed, dried, backfilled, rinsed again, and dried. Immediately thereafter, these samples were backfilled with MCU (10 μM in water) for 1 h to fill vacant gold sites, then rinsed again with water and dried with N_2. These samples were then immersed in target DNA solutions (1 nM ^{32}P-labeled oligonucleotide 2 diluted with unlabeled oligonucleotide 2) in 1× TE-NaCl buffer for 30 min, 1 h, and 2 h. Individual samples were removed at these three assay time points, rinsed copiously with 1× TE-NaCl buffer [a pure water rinse dissociates the DNA duplex (ref. 9 and data not shown)], dried with N_2, and exposed to a storage phosphor imager (Amersham Biosciences) simultaneously with [^{32}P]ATP standards for radioactivity surface measurements.

Grayscale pixelated images of surface ^{32}P density were obtained with a STORM (Amersham Biosciences) scanner and analyzed with ImageQuant version 5.1 software (Amersham Biosciences). Quantitation of sample DNA surface density using grayscale image analysis was performed by constructing calibration curves for each labeling reaction as described previously (15) and averaging two or three individual spots in each experiment. For studies of hybridization efficiency as a function of spot radial position, surface density profiles for both immobilized DNA probe and hybridized target were obtained from intensity line profiles drawn across the center of 2-mm-diameter spot ^{32}P-scanned images by using ImageQuant software. More than three spots (with two to four straight line profiles per spot) were analyzed for both DNA probe and target density profiles for each time point in each experiment.

Fluorescence Imaging of DNA Hybridization on Gold Spots. Plasma-cleaned substrates were immersed in DNA probe at 1 μM (5′-Cy3-olgo1-C3-SH-3′) in 1× TE-NaCl for 5 h, rinsed copiously with 1× TE-NaCl buffer and water, dried with N_2, then backfilled with aqueous 10 μM MCU for 1 h. After backfilling, rinsing, and drying, samples were then immersed in DNA target (1 nM 5′-oligo2-Cy5-3′) in 1× TE-NaCl buffer. Individual samples were removed at three assay time points (30 min, 1 h, and 2 h), rinsed copiously with 1× TE-NaCl buffer and then ice cold 0.1× TE-NaCl buffer, then dried with N_2. Ice-cold diluted buffer more effectively removes residual salt crystals from drying, which minimizes fluorescence scattering noise without any observable influence on double-stranded DNA yields. Samples were fluorescence scanned (ScanArray Express Imager, PerkinElmer, Fremont, CA) and then processed by using ImageQuant software.

Numerical Model. In this unstirred, quiescent system, DNA analyte transport through aqueous media to a discrete immobilized surface probe region occurs solely by diffusion due to the absence of forced or natural convection. (The quiescence assumption is warranted in this system, even for long experiment times. The 2-ml liquid sample fills the 22-mm diameter well to a depth of 5 mm, so the entire sample will thermally equilibrate with sudden external environmental changes in just over 10 s. The plate containing the wells is fixed and stationary, and analyte fluxes are not large enough to induce bulk flow. The system is sealed, preventing evaporative losses.) Once an analyte molecule reaches the surface where probe exists, it will reversibly hybridize at a finite rate, removing it from solution. The processes of analyte diffusion and solid-phase hybridization are described through a continuum species conservation equation and mass flux boundary condition, respectively. For the configuration being modeled, the equations are written in a boundary-fitted, orthogonal coordinate system known as oblate spheroidal coordinates (23), shown in SI Fig. 7. Further details on the coordinate system, the governing equations, and their solution are given in *SI Materials and Methods*.

Boundary Conditions. At the probe surface a mass balance is applied to relate the flux of target from the aqueous phase with the forward and reverse rates of hybridization. Several approaches have been used to formulate this condition, including its treatment as a thin disk into which analyte diffuses before reacting (24–26), but in many studies the spot is treated as a planar surface on which solid-phase hybridization occurs (27–29). In its simplest form the hybridization reaction may be treated as a one-step, reversible reaction between target and probe with rate constants k_1 and k_{-1} (30), which is the approach used here. In formulating the hybridization kinetics as described above, it is important to recognize that the hybridization details are masked by the assumed single-step sequence, and more important, the dissociation constant K_D may be two to 10 orders of magnitude different from the bulk solution hybridization value (30, 31).

Parameters. Model parameters were selected to match as close as possible the experimental conditions described above. A correlation exists for aqueous DNA oligomer diffusion coefficients (32), such that $D = 4.9 \times 10^{-6}\ bp^{-0.72}$ (cm^2/s), where bp is the number of base pairs. This correlation was applied because of evidence that the diffusion coefficients of relatively small ssDNA oligomers are not substantially different from those of double-stranded DNA oligomers of the same size (33). Based on a survey of multiple data (30) the dissociation constant K_D was chosen such that the solid phase hybridization value was three orders of magnitude larger than the bulk solution value; for this system the constant was chosen to be $K_D = 10^{-7}$ M, consistent with data in a recent study (34). The one adjustable parameter in the model is the forward rate constant k_1, because this kinetic solid-phase hybridization rate constant has not been measured for this specific system. A value found to reasonable is $k_1 = 10^3$ $M^{-1}{\cdot}s^{-1}$, which is several orders of magnitude lower than anticipated in bulk solution hybridization, $\approx 10^5$ to 10^6 $M^{-1}{\cdot}s^{-1}$ (30). The value of k_1 used here is consistent with that associated with the application of a one-step reversible reaction model (30, 35) to the normalized kinetics data (for 25-mers) in figure 5 of ref. 17. The significantly lower solid phase k_1 may be attributed, at least in part, to charge–charge interactions and steric hindrance. Last, the values of C_{To} and C_{Po} were taken from experiment; as noted in *Results*, it was necessary to incorporate the radial position dependence of C_{Po} into the model.

We thank D. Findley and J. Elzea for contributions to the numerical model development, P. Gong for technical advice, and N. Scott Lynn (Colorado State University) for fabricating gold spot arrays. This work was supported by National Institutes of Health Grant EB00726.

1. Ekins RP, Berger H, Chu FW, Finckh P, Krause F (1998) *Nanobiology* 4:197–220.
2. Ekins RP (1998) *Clin Chem* 44:2015–2030.
3. Shi L, Reid LH, Jones WD, Shippy R, Warrington JA, Baker SC, Collins PJ, de Longueville F, Kawasaki ES, Lee KY, Luo Y, *et al*. (2006) *Nat Biotechnol* 24:1151–1161.
4. Ekins RP, Chu FW (1991) *Clin Chem* 37:1955–1967.
5. Georgiadis R, Peterlinz KP, Peterson AW (2000) *J Am Chem Soc* 122:3166–3173.
6. Gong P, Harbers GM, Grainger DW (2006) *Anal Chem* 78:2342–2351.
7. Gong P, Lee, C-Y, Gamble LJ, Castner DG, Grainger DW (2006) *Anal Chem* 78:3326–3334.
8. Kimura-Suda H, Petrovykh DY, Tarlov MJ, Whitman LJ (2003) *J Am Chem Soc* 125:9014–9015.
9. Levicky R, Herne TM, Tarlov MJ, Satija SK (1998) *J Am Chem Soc* 120:9787–9792.
10. Petrovykh DY, Perez-Dieste V, Opdahl A, Kimura-Suda H, Sullivan JM, Tarlov MJ, Himpsel FJ, Whitman LJ (2006) *J Am Chem Soc* 128:2–3.
11. Rosi NL, Mirkin CA (2005) *Chem Rev* 105:1547–1562.
12. Shumaker-Parry JS, Zareie MH, Aebersold R, Campbell CT (2004) *Anal Chem* 76:918–929.
13. Steel AB, Levicky RL, Herne TM, Tarlov MJ (1999) in *218th ACS National Meeting* (Am Chem Soc, New Orleans).
14. Steel AB, Levicky RL, Herne TM, Tarlov MJ (1999) *Proc Electrochem Soc* 99–5:132–143.
15. Steel AB, Levicky RL, Herne TM, Tarlov MJ (2000) *Biophys J* 79:975–981.
16. Southern EM, Mir KU, Shchepinov MS (1999) *Nat Genet* 21:5–9.
17. Peterson AW, Heaton RJ, Georgiadis RM (2001) *Nucleic Acids Res* 29:5163–5168.
18. Wightman RM, Wipf DO (1989) in *Electroanalytical Chemistry*, ed Bard AJ (Dekker, New York), pp 267–353.
19. Saito Y (1968) *Rev Polarogr* 15:177–187.
20. Sapsford KE, Liron Z, Shubin YS, Ligler FS (2001) *Anal Chem* 73:5518–5524.
21. Mazzola LT, Frank CW, Fodor SPA, Mosher C, Lartius R, Henderson E (1999) *Biophys J* 76:2922–2933.
22. Forman JE, Walton ID, Stern D, Rava RP, Trulson MO (1998) *Am Chem Soc Symp Ser* 682:206–228.
23. Happel J, Brenner H (1965) *Low Reynolds Number Hydrodynamics* (Prentice–Hall, Englewood Cliffs, NJ).
24. Edwards DA (2001) *Bull Math Biol* 63:301–327.
25. Bhanot G, Louzoun Y, Zhu J, DeLisi C (2003) *Biophys J* 84:124–135.
26. Gadgil C, Yeckel A, Derby JJ, Hu W-S (2004) *J Biotechnol* 114:31–45.
27. Lagerholm BC, Thompson NL (1998) *Biophys J* 74:1215–1228.
28. Shvartsman SY, Wiley HS, Deen WM, Lauffenburger DA (2001) *Biophys J* 81:1854–1867.
29. Smart JL, McCammon JA (1998) *Biophys J* 75:1679–1688.
30. Levicky R, Horgan A (2005) *Trends Biotechnol* 23:143–149.
31. Tarlov MJ, Steel AB (2003) in *Biomolecular Films: Design, Function, and Applications*, ed Rusling JF (Dekker, New York), pp 545–608.
32. Lukacs GL, Haggie P, Seksek O, Lechardeur D, Freedman N, Verkman AS (2000) *J Biol Chem* 275:1625–1629.
33. Stellwagen E, Stellwagen NC (2002) *Electrophoresis* 23:2794–2803.
34. Vanderhoeven J, Pappaert K, Dutta B, Vanhummelen P, Baron GV, Desmet G (2004) *Electrophoresis* 25:3677–3686.
35. Henry MR, Stevens PW, Sun J, Kelso DM (1999) *Anal Biochem* 276:204–214.